Nanoscale Horizons

ROYAL SOCIETY OF CHEMISTRY

COMMUNICATION

View Article Online
View Journal | View Issue

Cite this: *Nanoscale Horiz.*, 2026, **11**, 883

Received 17th June 2025,
Accepted 6th January 2026

DOI: 10.1039/d5nh00424a

rsc.li/nanoscale-horizons

Green-synthesized gold-coated nanodiamonds as potential radiosensitizers for proton therapy

Edgar Mendes,[ab] Pietro Aprà,[c] Ana Belchior,[ad] Federico Picollo,[ce] Marta M. Alves,[fg] Rodica Mihaela Dinica,[h] Maria João Moura,[i] Sofia Sturari,[ce] Teresa Pinheiro *[bd] and Maria Paula Cabral Campello *[ad]

Nanodiamonds (ND) possess unique properties, including high biocompatibility, tunable surface chemistry, and stable photoluminescence, that make them highly attractive for biomedical applications. In this study, we synthesized gold-coated nanodiamonds (NDAu) using a green chemistry route based on *Nymphaea alba* root extract as a natural reducing agent. The hybrids were produced from two types of ND with median diameters of 50 nm and 230 nm, which were subjected to different thermal treatments prior to the gold coating to modulate their surface properties. The functionalized particles were comprehensively characterized using a combination of spectroscopic techniques (UV-Vis spectroscopy, ATR-FTIR spectroscopy, Raman spectroscopy, PIXE), Powder X-ray Diffraction (PXRD), electron microscopy (SEM and TEM), and zeta potential. These techniques evidenced the impact of the thermal treatments on the NDs, reported the influence of the plant extracts on the final nanoparticles, as well as confirmed and quantified the presence of metallic gold in this material. Moreover, we carried out biological evaluation on A549 lung cell line to assess their cytotoxicity, cellular uptake, and impact on cell survival. Our results confirmed the efficacy of the gold-coating method, elucidating the modifications in particles structural, physical and chemical properties due to functionalization, and the interaction with cells. These nanoparticles could then be used for various biomedical applications, such as drug delivery or as potential radiosensitizers.

New concepts

In this work, we present a novel and sustainable approach to synthesize hybrid gold-nanodiamond (NDAu) nanostructures using green chemistry principles. The final nanoparticles apart from retaining properties of nanodiamonds (such as photoluminescence), gained plasmonic and catalytic properties that enhance imaging, sensing, and therapeutic applications from the gold-coating. By employing *Nymphaea alba* root extracts as eco-friendly reducing and stabilizing agents, we successfully functionalized thermally treated nanodiamonds of two distinct sizes (50 nm and 230 nm) with gold, circumventing the use of toxic reagents or harsh conditions. To the best of our knowledge, this is the first report on the green synthesis of hybrid gold-coated nanodiamonds, which results in biocompatible, hybrid nanostructures with potential biomedical applications. Moreover, through a radiosensitization process, these gold-conjugated nanodiamonds could provide notable benefits in augmenting the effectiveness of radiation therapy, as well as having great contributions in imaging and photothermal therapy. All these finding led us to conclude that our work represents a significant advancement beyond previous studies that focused on nanodiamonds modified *via* conventional chemical routes. Our method not only introduces a sustainable alternative for NDAu synthesis but also opens new possibilities for tuning surface properties through natural phytochemicals.

[a] *Centro de Ciências e Tecnologias Nucleares, Instituto Superior Técnico, Universidade de Lisboa, Campus Tecnológico e Nuclear, Estrada Nacional 10, Km 139.7, 2695-066 Bobadela, Portugal. E-mail: edgar.mendes@tecnico.ulisboa.pt, anabelchior@ctn.tecnico.ulisboa.pt, pcampelo@ctn.tecnico.ulisboa.pt*

[b] *iBB-Institute of Bioengineering and Biosciences, Instituto Superior Técnico, University of Lisbon, 1049-001 Lisbon, Portugal. E-mail: teresa.pinheiro@tecnico.ulisboa.pt*

[c] *National Institute of Nuclear Physics, Section of Turin, Via P. Giuria 1, 10125 Turin, Italy. E-mail: pietro.apra@to.infn.it, federico.picollo@unito.it, sofia.sturari@unito.it*

[d] *Departamento de Engenharia e Ciências Nucleares (DECN), Instituto Superior Técnico, Universidade de Lisboa, Estrada Nacional 10, 2695-066 Bobadela, Portugal. E-mail: anabelchior@ctn.tecnico.ulisboa.pt, pcampelo@ctn.tecnico.ulisboa.pt*

[e] *Physics Department, and Nanomaterials for Industry and Sustainability (NIS) Inter-Departmental Centre University of Turin, Via P. Giuria 1, 10125 Turin, Italy. E-mail: federico.picollo@unito.it, sofia.sturari@unito.it*

[f] *Centro de Química Estrutural (CQE), Institute of Molecular Sciences (IMS), Instituto Superior Técnico, Universidade de Lisboa, Av. Rovisco Pais, 1049-001, Lisboa, Portugal. E-mail: martamalves@tecnico.ulisboa.pt*

[g] *Departamento de Engenharia Química (DEQ), Instituto Superior Técnico, Universidade de Lisboa, Av. Rovisco Pais, 1049-001 Lisboa, Portugal*

[h] *Faculty of Sciences and Environment, Department of Chemistry Physical and Environment, "Dunărea de Jos" University of Galati, 111 Domneasc̆a Street, 800201 Galati, Romania. E-mail: rodica.dinicas@ugal.ro*

[i] *Instituto Nacional de Investigação Agrária e Veterinária, I.P. - Laboratório Químico Agrícola Rebelo da Silva Tapada da Ajuda, P-1301-596 Lisboa, Portugal. E-mail: mjoao.mouras@iniav.pt*

Introduction

Today, cancer patients have numerous treatment options, with surgery, chemotherapy, and radiotherapy being the most common approaches. Surgery aims to completely remove the tumor but is typically feasible only in early stages or when the tumor is located in an operable area. It can also serve palliative purposes or involve partial tumor removal, often followed by chemotherapy or radiotherapy.[1] Chemotherapy uses cytotoxic agents to inhibit cell division and growth by causing genetic damage or blocking essential enzymes required for cell replication. However, its primary drawback is the lack of selectivity for cancer cells, leading to significant side effects and prompting efforts to develop more targeted treatments.[2] Radiotherapy, on the other hand, uses ionizing radiation—mainly X-rays—to destroy cancer cells or halt their proliferation. This radiation interacts directly with molecules, breaking bonds, or indirectly by generating Reactive Oxygen Species (ROS) that cause structural damage. These interactions often lead to DNA damage, including Single Strand Breaks (SSBs), Double Strand Breaks (DSBs), and base damage.[3] Despite the availability of these treatments, there is still no definitive cure for cancer. Classically, a combination of two or more strategies is employed to improve outcomes. Thus, ongoing research is critical to develop new and more effective therapies.

Proton therapy utilizes proton beams with a distinctive depth-dose profile that concentrates the radiation dose at the final microns of their path, forming a Bragg peak. This enables highly precise targeting of the radiation dose, minimizing harm to healthy tissues, unlike X-rays, which deliver their maximum dose to superficial tissues. However, proton therapy has a Relative Biologic Effectiveness (RBE) of 1.1, making it only 10% more effective than conventional radiation therapy.[4] Additionally, it requires costly equipment and specialized expertise. Despite these limitations, proton therapy is experiencing global growth, with over 100 operational facilities and over 50 under development.[5] Consequently, investigating new radiosensitizers—agents that enhance the biological impact of radiation—is vital to improving the efficacy of cancer therapy in general and proton therapy in particular.

Nanodiamonds (ND) are particularly attractive for biomedical applications due to their biocompatibility, ease of functionalization, and ability to penetrate biological barriers, offering potential solutions to the limitations of conventional approaches in cancer theranostics.[6–8] Their unique properties, such as the presence of Nitrogen Vacancy (NV) centers – characterized by a nitrogen atom substituting a carbon atom and a nearby lattice vacancy – further enhance their applicability in biomedical sciences. When excited with radiation in the range of 465 to 565 nm, the NV center emits light in the red spectrum, making NDs highly photostable with low photobleaching compared to common fluorescent dyes. This photoluminescent property, combined with the ability to induce additional NV centers, through high-energy particle irradiation followed by annealing at 600–800 °C, positions NDs as a valuable tool for bioimaging.[7–18]

NDs have garnered significant attention in research not only for their biomedical applications but also for their potential as radiosensitizers. Furthermore, nanodiamonds have been investigated for their ability to enhance radiosensitivity during proton and photon irradiation.[19–21] Additionally, surface modifications enable the conjugation of therapeutic agents, such as drugs or nucleic acids, and imaging probes, such as fluorophores or radiolabels, turning nanodiamonds into multifunctional platforms for targeted drug delivery and real-time disease monitoring.[6–8,22–27] A particularly promising modification involves the conjugation of gold onto the surface of nanodiamonds. Gold nanoparticles are well known for having exceptional surface and electronic properties, which make them perfect for a variety of biomedical applications.

The resulting composite—nanodiamond-gold hybrids---represents a cutting-edge development in nanotechnology, offering a synergistic combination of the unique properties of nanodiamonds and gold nanoparticles. NDs provide exceptional photostability, biocompatibility, and versatile surface chemistry, while gold nanoparticles contribute plasmonic and catalytic properties that enhance imaging, sensing, and therapeutic applications. This integration creates multifunctional systems with enhanced performance in bioimaging techniques, such as surface-enhanced Raman spectroscopy, photoacoustic imaging and multimodal imaging, leveraging the plasmonic properties of gold.[28–31] These hybrid nanoplatforms also demonstrate significant potential in biosensing and diagnostics, including immunosensors for the detection of cancer biomarkers like HER2, which exhibit high sensitivity and specificity in human serum samples.[32] Hybrid architectures, such as silica-encapsulated nanodiamonds coated with a gold shell, are effective in selective thermal ablation of cancer cells using near-infrared laser irradiation.[33] Additionally, their catalytic properties and DNA-based coupling mechanisms enable intracellular biosensing and therapeutic delivery, establishing nanodiamond-gold hybrids as versatile tools for advancing precision medicine.[34]

Through a radiosensitization process, gold-conjugated nanodiamonds provide notable benefits in augmenting the effectiveness of radiation therapy, in addition to their contributions to imaging and photothermal therapy. Because of their high atomic number (Z), which increases the local deposition of radiation energy, gold nanoparticles are well-established radiosensitizers. Gold can promote the generation of secondary electrons when applied to the surface of nanodiamonds, which increases DNA damage in cancer cells when exposed to ionizing radiation.[20,35–39] This effect is particularly advantageous for treating resistant tumors, where conventional radiation doses may be insufficient to achieve therapeutic outcomes. By leveraging gold's radiosensitizing properties, gold-functionalized nanodiamonds can potentially lower the required radiation dose, minimizing damage to surrounding healthy tissues while maintaining therapeutic efficacy. In proton therapy, AuNPs trigger mechanisms like the Coulomb nanoradiator effect and Auger cascades. Proton interactions with gold atoms strip electrons, generating reactive oxygen species (ROS) and X-rays, while secondary electron ejections *via* the Auger effect further increase tumor damage.[40–43] The physical, optical, and biological properties of nanoparticles strongly depend on their size, shape, surface functionalization, and the dielectric properties of their environment. These characteristics are intrinsically linked to the experimental conditions employed during their synthesis.[44]

Herein, we developed hybrid gold-nanodiamond (NDAu) nanostructures using two types of commercial NDs with median

sizes of 50 nm and 230 nm. The NDs were annealed at 800 °C for 2 hours in a nitrogen atmosphere, yielding annealed nanodiamonds (Ann NDs 50 and Ann NDs 230). These were subsequently oxidized in air at 500 °C for 12 hours, producing oxidized nanodiamonds (Ox NDs 50 and Ox NDs 230).[20] The gold coating on the NDs was synthesized using green chemistry methods with *Nymphaea alba* root extracts as reducing agents, in line with sustainable practices. *Nymphaea alba*, also known as the European white-water lily, is rich in phytochemicals whose composition varies by geographical location and plant part. These extracts are known for their antioxidant, anti-inflammatory, and hepatoprotective properties, as well as their traditional use in treating diabetes, urinary tract infections, and other ailments. The key bioactive effects are largely attributed to polyphenols such as ellagic acid and flavonoids like quercetin and kaempferol.[45,46]

Green chemistry emphasizes reducing the environmental and health impacts of nanoparticle production by avoiding toxic solvents and pollutants. It leverages biological molecules such as polyphenols, citric acid, flavonoids, and reductases found in plants, algae, or microorganisms.[45–49] These methods are versatile, cost-effective, and can incorporate biological waste from agricultural or food industries, lowering the carbon footprint of nanoparticle synthesis. Furthermore, green nanoparticles exhibit improved biocompatibility, as harmful chemical contaminants are avoided. Organic compounds from plant extracts integrated into the nanoparticle surfaces can enhance cellular uptake and confer additional beneficial properties, such as antimicrobial or anticancer activity.[50]

While green chemistry has been widely used to produce metal or metal oxide nanoparticles, to our knowledge, this is the first report of hybrid gold-nanodiamonds synthesized using this approach. Comparable methods, such as the environmentally friendly synthesis of silver nanoparticles on nanodiamonds using tea polyphenols, have demonstrated the potential of such strategies.[50] Hybrid metal-ND for multipurpose biological applications, such as imaging or for hyperthermia, have also been synthesized using conventional chemical methods.[39]

In this study, the synthesized hybrid gold-nanodiamond underwent comprehensive physicochemical characterization. Their biological activity was preliminarily evaluated through cytotoxicity assays, cell survivability and colony formation assessments, and cellular uptake studies. These evaluations were conducted using the A549 lung cancer cell line, since it is a critical cancer located near vital structures, complicating treatment due to the risk of damaging healthy tissues. Moreover, these cancers often exhibit resistance to conventional therapies, underscoring the need for innovative and targeted treatment approaches.[51,52] These biological assays were intended as a first assessment of cytocompatibility, supporting future in-depth biomedical investigations.

Materials and methods

Reagents and materials

All chemicals and solvents were of reagent grade and were used without additional purification, unless stated otherwise. The Milli-Q water was produced from a Millipore system Milli-Q $\geq$18 MΩ cm (with a Millipak membrane filter 0.22 μm). Tetrachloroauric(III) acid trihydrate 99% ($HAuCl_4 \cdot 3H_2O$) and sodium hydroxide (NaOH) were commercially acquired from Aldrich Chemical. The roots of the Danube Delta *Nymphaea alba* species were obtained from the Biosphere Reserve of Romania and Environment, Department of Chemistry Physical and Environment, ''Dunărea de Jos'' University of Galati.[47]

The A549 lung carcinoma epithelial cell was purchased from the American Type Culture Collection. The cell lines were cultured in Dulbecco's Modified Eagle Medium supplemented with 10% fetal bovine serum (FBS), supplemented with 1% of antibiotic–antimycotic solution. The cells were kept at 37 °C and 5% CO_2 in a humidified atmosphere (Heraeus, Germany). All products for cellular studies, including the cellular media and supplements, were acquired from Gibco (Thermo Fisher Scientific), unless otherwise stated.

Synthesis of Gold-coated nanodiamonds (NDAu)

Thermal treatment of the NDs. Two types of commercially available NDs, MSY 0-0.1 and MSY 0-0.5, with average sizes of 50 nm and 230 nm respectively, were employed in this study. All samples were supplied by Pureon. Initially, both ND types underwent a high temperature thermal annealing treatment at 800 °C for 2 h under nitrogen flow. The annealed nanodiamonds were labelled Ann ND 50 and Ann ND 230. Subsequently, a portion of the annealed samples was subjected to thermal oxidation in air at 500 °C for 12 h to selectively remove the graphitic outer layers and modulate the surface oxidation state.[53] This process yielded the oxidized samples Ox ND 50 and Ox ND 230. All thermal treatments were carried out using a ThermoConcept ROT 60/300/12 tubular furnace.[54]

Processing of the root extract used for the synthesis of the gold-coating. Root extracts from *Nymphaea alba* were utilized to synthesize the gold coating on nanodiamonds.[45,47–49] A stock solution of the root extracts was prepared to be used in the gold coating synthesis process of the NDs. 2 g of powder root extracts were dispersed in 120 mL of Milli-Q water and stirred during 1 h at 30 °C. The obtained extract suspension was cooled to room temperature and twice filtered through a Whatman No. 1 filter paper. The filtered yellow extract was used immediately to prevent any changes in its composition or loss of reactivity, which is crucial for the gold coating process on the nanodiamonds.

General procedure for the gold-coating. The NDs were dispersed in 25 mL of separate root extract solutions and subjected to ultrasonic irradiation for 10 minutes at room temperature, using an ultrasonic batch (Fisherbrand TM S-Series FB15051) operating at 38 kHz and 100 W. This was followed by magnetic stirring for an additional 40 minutes. After stirring, a 25 mM $HAuCl_4$ water solution was introduced, causing the reaction mixture to immediately change color from bright yellow to brown. Then, a 0.1 M NaOH solution was added dropwise until the pH reached 8. At this point, a second volume of 25 mM $HAuCl_4$ water solution was gradually added while stirring at room temperature, leading to a color change from brown to gray-blue. The samples were incubated overnight at room temperature with

Table 1 Type of modified NDs, ND precursor and volume of gold added

Sample	Precursor	Volume of $HAuCl_4$ (mL)
Ann NDAu 50	28 mg Ann ND 50	2 + 8
Ox NDAu 50	27 mg Ox ND 50	2 + 8
Ann NDAu 230	18 mg Ann ND 230	1.5 + 4.5
Ox NDAu 230	17 mg Ox ND 230	1.5 + 4.5

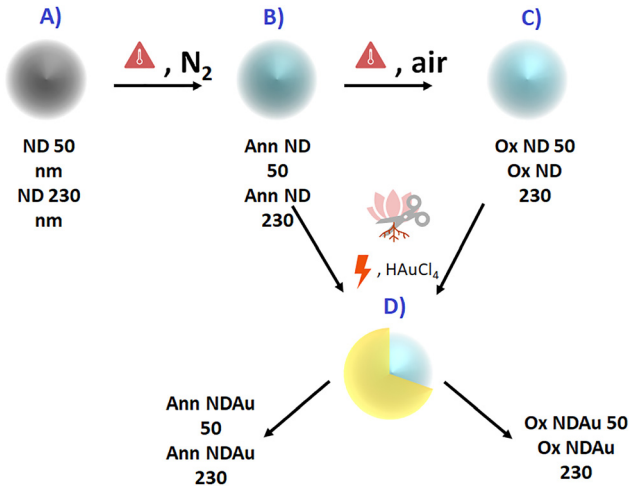

Scheme 1 Synthesis steps of the gold-coated nanodiamonds. (A) Commercial NDs of 50 and 230 median diameters were purchased and (B) were thermally annealed at 800 °C in a N2 atmosphere (Ann NDs). (C) A portion of the Ann NDs were oxidized in air at 500 °C (Ox NDs). (D) Both Ann and Ox NDs were gold-coated by employing root extracts of *Nymphaea alba* as a gold reducing agent (Ann and Ox NDAu).

continuous magnetic stirring. After incubation, the solutions were washed twice with Mili-Q water at 6000 RPM for 20 minutes and then freeze-dried for 48 hours.

Table 1 lists the acronyms for each gold-coated ND and the specific amounts of reagents and precursors used at each synthesis step, and an outline of the different synthesis stages is also provided in Scheme 1, which includes the starting nanodiamonds (A), thermal pretreatment (B), surface oxidation (C), and gold reduction with Nymphaea alba root extract (D).

NDAu characterization

NDAu characterization involved ultraviolet-visible spectroscopy (UV-Vis), Powder X-ray diffraction (PXRD), dynamic light scattering (DLS) and zeta potential (ζ-potential), attenuated total reflectance-fourier transform infrared (ATR-FTIR), particle-induced X-ray emission (PIXE), Raman spectroscopy, scanning electron microscopy (SEM) and transmission electron microscopy (TEM). UV-Vis spectra were recorded in water from 200–900 nm using a Varian Cary 50 UV/Vis spectrophotometer at room temperature. PXRD analysis was performed with a Bruker D2 Phaser diffractometer, equipped with a Cu Kα X-ray tube, in the 2θ range from 10° to 100°, with crystal size and parameters calculated using Scherrer's equation.[55] ζ-potential measurements utilized a Malvern Zetasizer Nano ZS operating at a 173° angle with a 633 nm He-Ne laser. ATR-FTIR spectra were obtained using a Thermo Fisher Scientific FTIR Nicolet iS50 spectrometer with an ATR diamond crystal accessory. Elemental quantification of carbon was determined by dry combustion on a Thermo Unicam Flashsmart® NCS analyser at National Institute for Agrarian and Veterinary Research and the gold elemental quantification was performed by PIXE analysis using a 2 MeV proton beam from the 2.5 MeV Van de Graaff accelerator at CTN/IST, after acid digestion (1 : 3 nitric to hydrochloric acids molar ratios) of NDAu samples. Raman spectra were acquired with a Horiba LabRAM HR800 Evolution using a 532 nm solid-state laser at 20 mW output power. SEM analysis was conducted using a Phenom ProX G6 or Hitachi S-2400, operating with an electron beam at 15 or 20 kV, respectively. TEM imaging was performed on a JEOL 1200EX and the size distribution and mean diameter of the annealed and oxidized NDAu samples were assessed.

Cell studies

Cytotoxicity studies and Cell Survival. The cytotoxicity of NDAus was evaluated using the colorimetric assay 3-[4,5-dimethylthiazol-2-yl]-2,5 diphenyl tetrazolium bromide-MTT assay, at concentrations of 10, 20, 50 and 100 μg mL^{-1} in the A549 cell line, with absorbance measured at 570 nm using a Varioskan LUX scanning multimode reader (ThermoFisher Scientific, US). To address the intrinsic absorbance of NDAus, a luminescence-based ATP assay kit (Sigma-Aldrich) was also used to evaluate cytotoxicity at the same range of concentrations in the A549 cells with luminescence measured on the same instrument. All experiments were performed in triplicate.

Cell survival. A clonogenic assay was performed to evaluate cell survival after treatment with NDAus alone or following proton irradiation. A549 cells were seeded at a density of 1000 cells per well in 24-well plates and incubated overnight to allow adhesion. The cells were then treated with 10 or 20 μg mL^{-1} of Ox NDAus for 24 hours. Irradiated cells were trypsinized and reseeded in fresh medium. After a 7-day incubation, the cells were fixed and stained with a Giemsa's azur-eosin-methylene blue solution (5% v/v in buffer). Colonies were manually counted to determine the surviving fraction (SF). All experiments were performed in triplicate.

Cell irradiation with protons. A549 cells, either treated with NDAus or untreated (controls), were irradiated at the external microbeam facility of the CTN/IST Van de Graaff accelerator. The irradiation geometry and dose calculations, performed using a Monte Carlo (MC) method, are described in detail elsewhere.[56] Briefly, a focused 2.0 MeV proton beam was raster-scanned over the cell monolayer (1000 cells seeded and incubated in 24-well plates) positioned perpendicular to the beam path. The proton energy was adjusted by varying the air path length and introducing Mylar® foils as attenuators to position the Bragg peak region within, though not entirely confined to, the cell layer (estimated H_2O-equivalent thickness of 30 μm). Cells were irradiated for 3 s, corresponding to a total absorbed dose of 17 Gy.

Cellular uptake studies. To evaluate NDAu cellular uptake, A549 cells were seeded on 100 nm thick silicon nitride membranes, allowed to adhere overnight, and incubated for

24 hours in medium containing either Ann NDAu 50 or Ox NDAu 50 at a concentration of 20 μg mL^{-1}. After incubation, cells were washed with cold PBS and freeze-dried. Gold distribution within the cells was analysed using particle-induced X-ray emission (PIXE) and elastic backscattering spectrometry (EBS) techniques at the nuclear microscopy facility of the Van de Graaff accelerator (CTN/IST). Data acquisition, spectrum processing, and concentration calculations were performed with the OMDAQ-3 program, with elemental concentrations reported as %(m/m) dry weight.[57]

Results and discussion

Surface modification of NDs and NDAus

Commercial NDs of two sizes (50 nm and 230 nm) were evaluated, each subjected to distinct thermal treatments. One set was annealed at 800 °C for 2 hours in a nitrogen (N_2) atmosphere, producing annealed nanodiamonds (Ann ND 50 and Ann ND 230). This process aimed to reorganize the disordered sp^2/sp^3 carbon phases and to graphitize the amorphous carbon shells while preserving the diamond core structure. The use of a nitrogen atmosphere prevented oxidation-related etching of the diamond lattice, which is known to occur at temperatures above 500 °C in the presence of oxygen.[17] A portion of these was further oxidized in air at 500 °C for 12 hours, generating oxidized nanodiamonds (Ox ND 50 and Ox ND 230). This study explored the potential of *Nymphaea alba* root extracts to synthesize and stabilize AuNPs directly on the ND surface, leveraging the extracts as a green reducing agent for the *in situ* reduction of $HAuCl_4$ and stabilization of the nanoparticles, resulting in a well-distributed NDAu hybrid nanoplatform. The Ox ND exhibited significantly improved dispersibility in water, likely due to the higher presence of oxygen-containing functional groups on its surface, which enhanced interactions with the reaction medium and contributed to the greater mass of the Ox NDAu nanoplatforms. In contrast, the Ann NDAu nanoplatforms showed a lower mass compared to the Ox NDAu counterparts, particularly for the larger 230 nm particles, despite equivalent amounts of gold precursor and root extract being used (see Table S1).

The effectiveness of *Nymphaea alba* root extracts in promoting the green-synthesis of gold coated nanodiamonds was demonstrated through a comprehensive set of complementary techniques. UV-vis, infrared, and Raman spectroscopies together with powder X-ray diffraction (PXRD), proton induced X-ray emission (PIXE), scanning electron microscopy (SEM), transmission electron microscopy (TEM), and measurements of DLS and zeta potential, consistently revealed changes in surface chemistry and morphology. Altogether, these results confirmed the efficiency *in situ* formation of the gold coating process on various nanodiamonds types, validating the extracts' dual role as both reducing and stabilizing agents in the synthesis process.

It is anticipated that NDs' poorly absorbing particles will have UV-vis spectra that are strongly influenced by λ^4, resulting in a curve that is more akin to exponential decay, with absorbance rising quickly as wavelength drops, especially in the UV region.[58] The UV-Vis spectra of Ann NDAu 50 and Ox NDAu 50 exhibit a distinct absorption band at 545 nm, indicative of gold nanoparticle formation *via* localized surface plasmon resonance (LSPR).[51] In the spectra of Ann NDAu 230 and Ox NDAu 230, this band is red-shifted to approximately 550 nm, consistent with the formation of larger nanoparticles and/or the presence of aggregates. Additionally, all NDAu samples exhibit absorption bands below 300 nm, which are attributed to polyphenolic and flavonoid compounds originating from the *Nymphaea alba* root extracts. This spectral feature supports the involvement of these phytochemicals in both the reduction of gold ions and the stabilization of the resulting nanoparticles.[46] These findings are corroborated by the FTIR and UV-Vis spectra shown in Fig. 1 for the pristine and gold-coated Ann ND 50 samples. Corresponding spectra for the remaining samples are provided in Fig. S1 and S2.

The FTIR spectra of the pristine nanodiamond samples exhibit characteristic stretching and bending vibrations associated with annealed or oxidized NDs. Key absorption bands

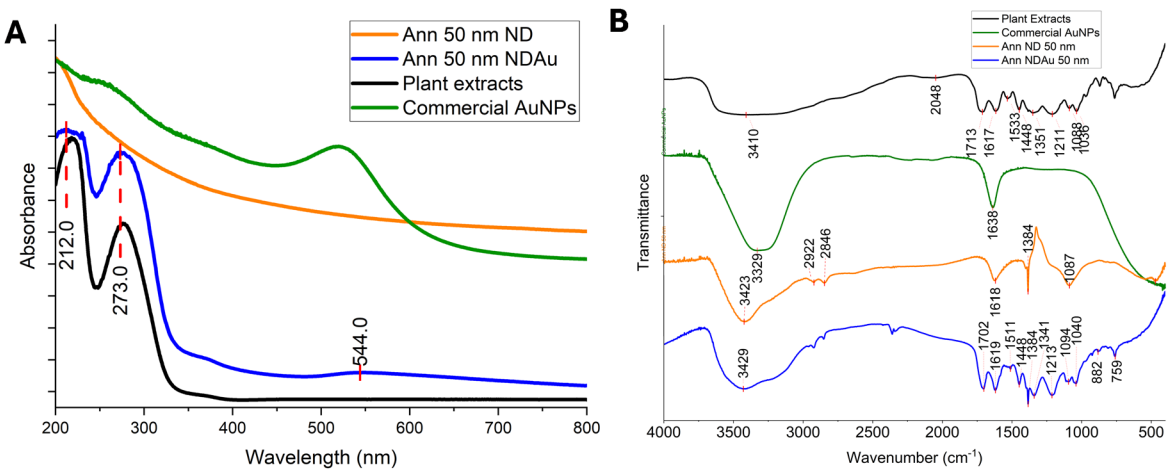

Fig. 1 (A) UV-Vis and (B) FTIR spectra of 50 nm Ann ND, Ann NDAu, plant extracts and commercial AuNPs.

include a broad peak at 3420 cm^{-1} (O–H stretch of water), 1618 cm^{-1} and 1630 cm^{-1} (O–H bending), 1384 cm^{-1} (C–N stretching), and 1090 cm^{-1} and 1110 cm^{-1} (C–O stretching).[59,60] The C–N band at 1384 cm^{-1} is less prominent in the Ox NDs, compared to the annealed counterpart, indicating effective nitrogen removal. The Ann ND shows smaller bands at 2920 cm^{-1} and 2849 cm^{-1} (CH_2 stretching), while the Ox ND has unique bands at 1774 cm^{-1} (C═O stretching from ketones) and 1263 cm^{-1} (C–O bending from esters). In the NDAu spectra new peaks emerge at 1700 cm^{-1} (C═C stretching of carboxylic acids) and 1445 cm^{-1} (C–O–H bending flavonoids), which align with the presence of polyphenols and flavonoids, such as ellagic acid and quercetin, reported as key (C–O of flavonoids), consistent with the presence of polyphenols such as ellagic acid and quercetin, previously identified in *N. alba* root extracts.[45] Additional peaks at 1582 cm^{-1} and 1508 cm^{-1} (aromatic C═C stretching) and 1366 cm^{-1} (O–H bending of phenolic groups) further support the successful contribution of these phytochemical components present in the extracts not only as a reducing, but also as a source of functional groups that enhance the stability and bioactivity of the hybrid nanostructures. The presence of esters and polyols, evidenced by the bands at 1111 cm^{-1} and 1200 cm^{-1}, respectively, reinforce the involvement of plant-derived molecules in surface functionalization, potentially improving the biomedical applicability of the resulting nanodiamonds.[45,46,59,60] Although metal NPs should not have any characteristic FTIR bands, an ATR-FTIR spectrum was recorded for commercial AuNPs (Aldrich Chemistry, 5 nm diameter) stabilized in citrate buffer in order to verify that neither of the bands in the NDAu samples arise from the gold in the surface. As expected, the only bands present in the AuNPs spectrum correspond to the O–H stretching of water and a C═O symmetrical stretching from the citrate molecule.[61]

Fig. 2 shows the Raman spectra of the 50 nm pristine nanodiamonds and their gold-coated counterparts. As shown in Fig. 2A and B, the spectra of the pristine NDs display features characteristic of this type of material: the diamond peak (red) at around 1320 cm^{-1}, which corresponds to sp^3 bonded carbon; the D band (green) at 1330–1340 cm^{-1}, indicating defects or disordered sp^2 carbon; and the G band (light blue) at around 1590 cm^{-1}, related to in-plane sp^2 carbon (graphite-like carbon). The diamond peak is usually located at 1332 cm^{-1}, but it can be shifted to lower Raman shifts in the case of nanodiamonds.[62] A fourth band, the D'' band (dark blue), is associated to defects probably located on the nanodiamond surface.[59–61] In the case of the gold-coated nanodiamonds, peak fitting was not performed due to a marked loss in Raman signal. This attenuation arises from the gold coating, which does not produce a Raman signal and reduces the overall signal intensity through light absorption, scattering and refraction. Notably, the diamond peak was significantly diminished or absent, confirming the presence of a gold layer coating on the nanodiamonds.

The Raman spectra for the 230 NDs and corresponding NDAus are shown in Fig. 3. Interestingly, unlike other NDAu samples, the Ann NDAu 230 sample retains a noticeable diamond peak (Fig. 3C), likely less influenced by the gold shell, which alters Raman signals. This suggests that the Raman signal may still be partially transmitted through a thinner or less uniform gold shell. Supporting this hypothesis, the gold content determined by PIXE analysis (Table 4) shows that this sample contains

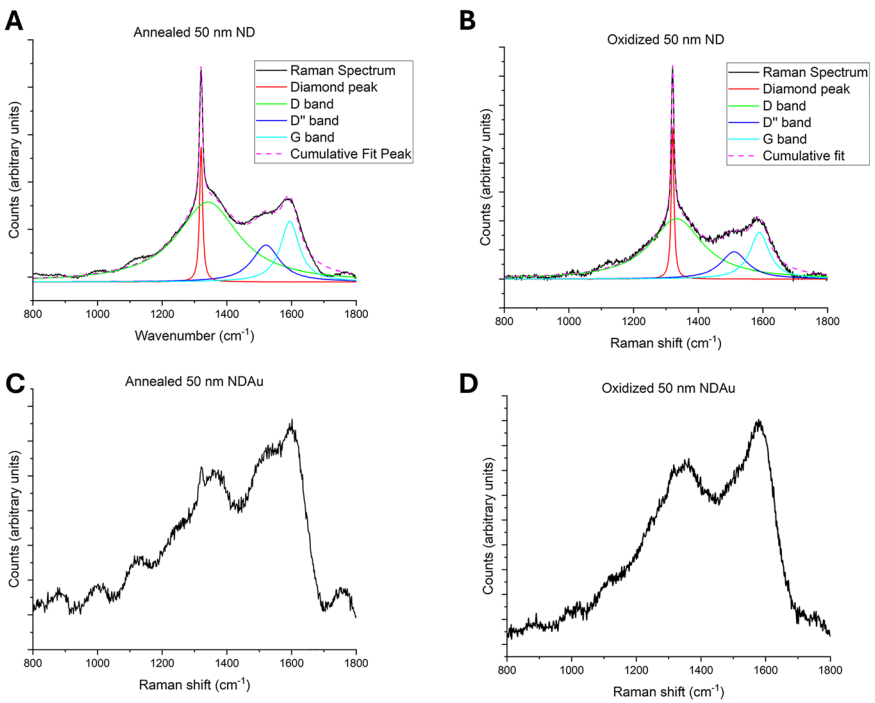

Fig. 2 Raman spectra of 50 nm (A) Ann ND, (B) Ox ND, (C) Ann NDAu and (D) Ox NDAu. In unmodified nanodiamond spectra (A) and (B), 4 curves were deconvoluted from the spectra into the D peak (red), the D band (green), D″ band (dark blue) and G band (light blue).

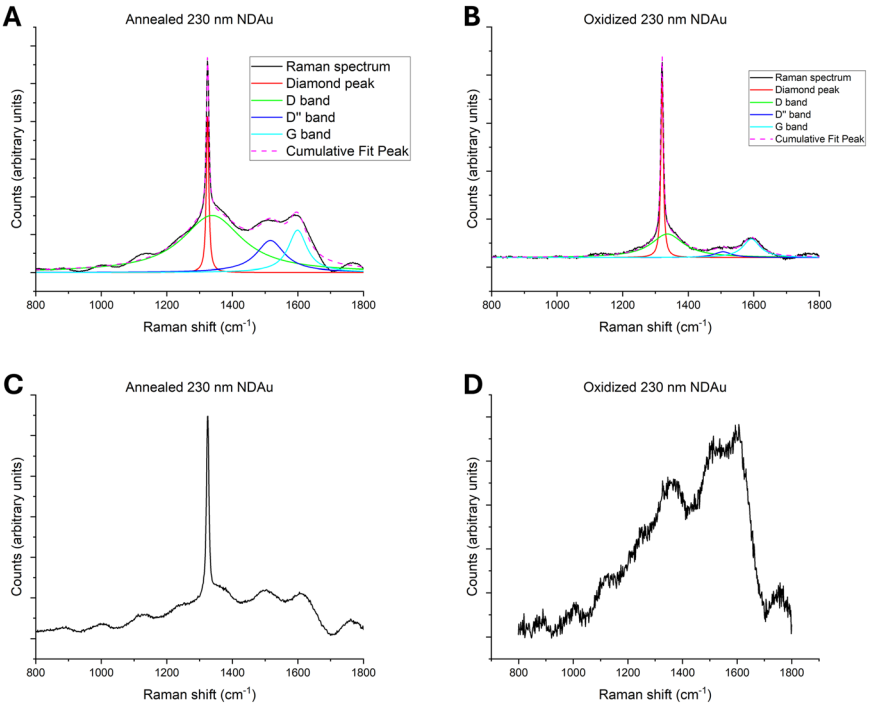

Fig. 3 Raman spectra of 230 nm (A) Ann ND, (B) Ox ND, (C) Ann NDAu and (D) Ox NDAu. In unmodified nanodiamond spectra (A) and (B), 4 curves were deconvoluted from the spectra into the D peak (red), the D band (green), D″ band (dark blue) and G band (light blue).

a comparatively lower amount of gold on the surface. These results point to an inverse correlation between the intensity of the diamond band and the surface gold content, with the Raman signal detection in NDAu systems supporting altered thickness and uniformity of the green synthesised gold layer.

Furthermore, Fig. 3B illustrates the effects of the oxidation process on nanodiamonds following annealing. The D and G bands are considerably less intense than the diamond peak after oxidation treatment, indicating effective removal of surface sp^2 carbon species, including graphitic domains and amorphous carbon. This confirms that the oxidation process successfully eliminates non-diamond carbon and residual organic contaminants from the ND surface, enhancing the purity of the sp^3 carbon core.

Table 2 presents the ratios derived from the deconvoluted Raman spectra of the 50 nm and 230 nm nanodiamonds, providing insights into their carbon structure. These ratios, calculated from the maxima of each deconvoluted peak, reflect the contributions of different carbon species. Specifically, the ratios of the diamond peak to the G band and the diamond peak to the D band indicate the sp^3/sp^2 ratio, while the D-to-G ratio relates to the structural ordering of sp^2 carbon.[63] The data clearly show that the oxides of NDs exhibit a higher diamond Raman signal than sp^2-phase carbon. This confirms the efficacy of the oxidation process in selectively etching the graphitic shells. The D-to-G ratio, which decreases as sp^2 carbon becomes more ordered, shows minimal variation through the samples. All ND batches underwent an annealing process to promote the conversion of amorphous carbon phases into graphitic ones, to standardise the surface terminations, and to facilitate the oxidation process. This results in comparable ratios for all the analysed NDs, with only a minimal decrease after oxidation at 500 °C.[63,64] Notably, the changes in the diamond peak ratios are more pronounced in the 230 nm NDs than in the 50 nm NDs. While the 50 nm samples exhibit approximately a 50% increase in the diamond peak to G band ratio after oxidation (from 1.50 to 2.52), the 230 nm samples demonstrate a more significant increase of around 160% (from 2.79 to 7.63), indicating a higher relative quantity of sp^3-bonded carbon compared to sp^2-bonded carbon in the larger samples. The greater size of the 230 nm NDs likely contributes to their higher diamond peak ratios in the annealed samples (Ann NDs), as the innermost regions of these larger particles were less affected by the annealing conditions, preserving more of the diamond core. In the Ox NDs, the D-to-G ratio decreases slightly as a result of the oxidation process. This decrease reflects a reduction in disordered sp^2 carbon, which is attributed to superficial etching that selectively enhances the sp^3-dominant diamond signal.

To assess the crystallinity and grain size of the nanodiamonds and their gold-coated counterparts, powder X-ray

Table 2 Raman intensity ratios for the 50 and 230 nm NDs

Sample	Diamond peak / G band	Diamond peak / D band	D band / G band
Ann ND 50	1.70	2.24	1.32
Ox ND 50	2.52	3.27	1.30
Ann ND 230	2.79	3.76	1.35
Ox ND 230	7.63	9.67	1.27

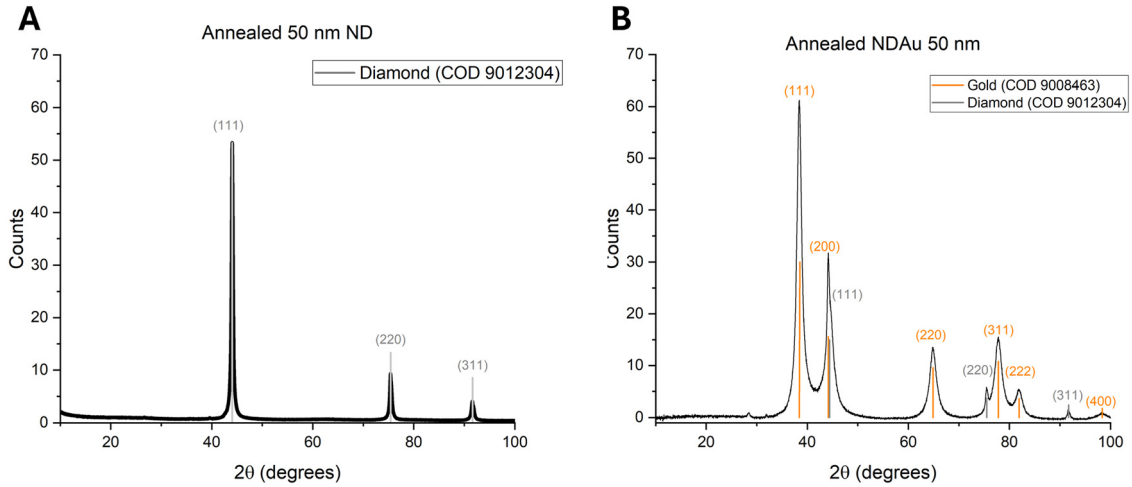

Fig. 4 XRD pattern of 50 nm (A) Ann ND 50 nm, (B) Ann NDAu 50 nm.

Table 3 PXRD characterization of the 50 nm and 230 nm NDs and NDAus

Sample	Phase	Lattice parameter (Å)*	2θ (°)	Crystallite size (nm)
Ann ND 50	Diamond	3.56	44.04	23.67 ± 0.06
Ox ND 50	Diamond	3.56	44.04	24.92 ± 0.11
Ann ND 230	Diamond	3.56	44.05	33.85 ± 0.09
Ox ND 230	Diamond	3.56	44.04	36.81 ± 0.11
Ann NDAu 50	Metallic Au	4.07	38.43	7.31 ± 0.02
Ox NDAu 50	Metallic Au	4.07	38.43	7.76 ± 0.02
Ann NDAu 230	Metallic Au	4.07	38.34	12.41 ± 0.02
Ox NDAu 230	Metallic Au	4.07	38.32	11.49 ± 0.02

diffraction (PXRD) was performed on these samples within the 2θ range of 10° to 100° (Fig. 4 and Fig. S3). The PXRD patterns of the nanodiamonds (NDs) exhibit characteristic diffraction peaks, which can be indexed to the diamond crystal planes (111), (220), and (311), at approximately $2\theta = 44°$, $2\theta = 75°$, and $2\theta = 91°$, respectively (Table 3). These values are consistent with the Crystallography Open Database (COD 9012304) and confirm the pure crystalline nature of annealed and oxidized NDs, with no other crystalline phases detected.[65,66]

For the NDAus, the PXRD patterns reveal eight diffraction peaks. Three of these correspond to the crystal planes of diamond, while the remaining five are indexed to the (111), (200), (220), (311), and (222) lattice planes, characteristic of the face-centered cubic (FCC) structure of metallic gold, in agreement with the Crystallography Open Database (COD 9008463). The patterns confirm the purity of the samples, with no crystalline impurities detected.

Using Scherrer's equation, the crystallite sizes were estimated based on the highest-intensity diffraction peaks. For the gold coating, the crystallite sizes were 7.31 nm and 7.76 nm for the Ann NDAu 50 and Ox NDAu 50 samples, respectively. In the NDAu 230 samples, larger gold crystallite sizes were observed: 12.41 nm for the annealed and 11.49 nm for the oxidized variants, respectively. These values are in good agreement with those reported in the literature for gold nanoparticles synthesized *via* green chemistry approaches.[66] The diamond crystallite sizes in the Ann ND 50 and OX ND 50 were 23.67 nm and 24.92 nm, respectively, while the values increased to 33.85 nm and 36.81 nm for the Ann ND 230 and Ox ND 230 samples, respectively. These differences may reflect the influence of particle size and surface treatments on the diffraction profile. It is important to note that the crystallite size reflects the dimensions of coherent diffracting domains and not necessarily the full physical size of the particles. Deviations between crystallite and particle sizes may arise from the presence of amorphous regions, surface defects, or polycrystalline structures, particularly in the case of coated or functionalized nanoparticles. Additional details regarding the diffraction peaks and crystallite size calculations for additional lattice planes are provided in Tables S2 and S3.

PIXE analysis revealed variations in the composition of the modified nanodiamonds between annealed and oxidized samples. Table 4 presents the mass percentages of gold in the NDAu samples, as determined by PIXE, along with the relative carbon content of both pristine and gold-coated nanodiamonds, determined through dry combustion. These carbon measurements provide additional insight into the extent of surface modification and gold deposition. In general, a decrease in the carbon content after gold coating was observed, which is consistent with the incorporation of heavier elements on the nanodiamond surface.

Table 4 Carbon and gold relative compositions in NDs and NDAus, respectively, determined by dry combustion and PIXE

Nanodiamond	Mean C[a] (w/w%)	Mean Au[b] (w/w%)
Ann ND 50	95.42	
Ox ND 50	69.07	
Ann ND 230	99.03	
Ox ND 230	81.71	
Ann NDAu 50	42.64	37.34 ± 0.06
Ox NDAu 50	40.60	39.50 ± 0.04
Ann NDAu 230	35.45	19.62 ± 0.13
Ox NDAu 230	45.93	41.06 ± 0.06

[a] Determined by dry combustion. [b] Determined by PIXE.

Trace amounts of other elements, such as calcium, iron, and potassium, were also detected (Table S4), but their contributions were minimal and did not significantly affect the elemental balance.

The PIXE technique, based on the emission of characteristic X-rays following the relaxation of electron clouds excited by energetic proton beams from a particle accelerator, allows for precise multi-elemental analysis. The low error values for all gold measurements ($<0.2\%$) underscore the high analytical precision of the method.

Regarding the NDAu 50 samples, the gold content was slightly higher in the oxidized material (39.50%) compared to the annealed one (37.34%), although the values were relatively close. This minor discrepancy may be attributed to the oxidized nanodiamonds presenting a higher density of oxygen-containing functional groups, which likely enhanced their interaction with the gold-containing reaction bath, promoting more effective adsorption and deposition of gold ions.

In contrast, more pronounced differences were observed for the NDAu 230 samples. The oxidized material exhibited a significantly higher gold content (41.06%) compared to its annealed counterpart (19.62%), more than doubling the amount of deposited gold. The carbon content measurements also reflect this trend, with a more substantial reduction in carbon content after oxidation and coating, consistent with a more extensive surface modification. These results highlight the critical role of oxidative treatment in preparing the surface of larger nanodiamonds for efficient gold deposition. The markedly lower gold content in the annealed sample may be associated with incomplete surface coverage, reduced gold–nanodiamond interaction due to residual surface contaminants, or insufficient surface activation. Conversely, oxidation likely removed such impurities and introduced polar functional groups, increasing the reactivity of the surface.

Another factor that may have contributed to the improved gold deposition on oxidized samples is their enhanced hydrophilicity. Compared to annealed nanodiamonds, which tend to be more hydrophobic, the oxidized surfaces exhibit a greater affinity for aqueous environments. This increased wettability could facilitate more intimate contact between the nanodiamond surface and the plant-derived aqueous reaction medium, thereby improving the efficiency and uniformity of gold ion adsorption and subsequent reduction. Taken together, these observations suggest that the chemical nature of the nanodiamond surface alone does not fully account for the differences in gold uptake. Physical parameters, such as particle size and surface-to-volume ratio, also play a critical role. These trends underscore the influence of particle size and surface-to-volume ratio on gold deposition. Smaller particles (50 nm), with their higher surface-to-volume ratios, appear to support more uniform gold coverage under both annealing and oxidation conditions. Larger particles (230 nm), however, seem to require oxidative treatment to expose sufficient reactive surface for comparable gold deposition. These results highlight the importance of surface chemistry and treatment methods in tailoring gold content and coating quality in nanodiamond modifications, particularly for applications that require precise control over coating properties, such as drug delivery, radiosensitization, or catalysis.

To further investigate these trends, SEM and TEM analyses were performed to characterize the morphology and size distribution of green-synthesized hybrid gold-nanodiamonds, focusing on their shape and size distribution. Fig. 5 shows representative SEM (A–D) and TEM (E–H) images of the NDAu samples. The images indicate that NDAu tend to form small aggregates, which are more evident in the annealed samples. The corresponding particle size distributions of the NDAu samples are reported in Fig. 6.

The direct *in situ* synthesis of gold nanoparticles in a nanodiamond dispersion typically produces spherical or quasi-spherical particles. SEM and TEM images indicate that numerous small gold

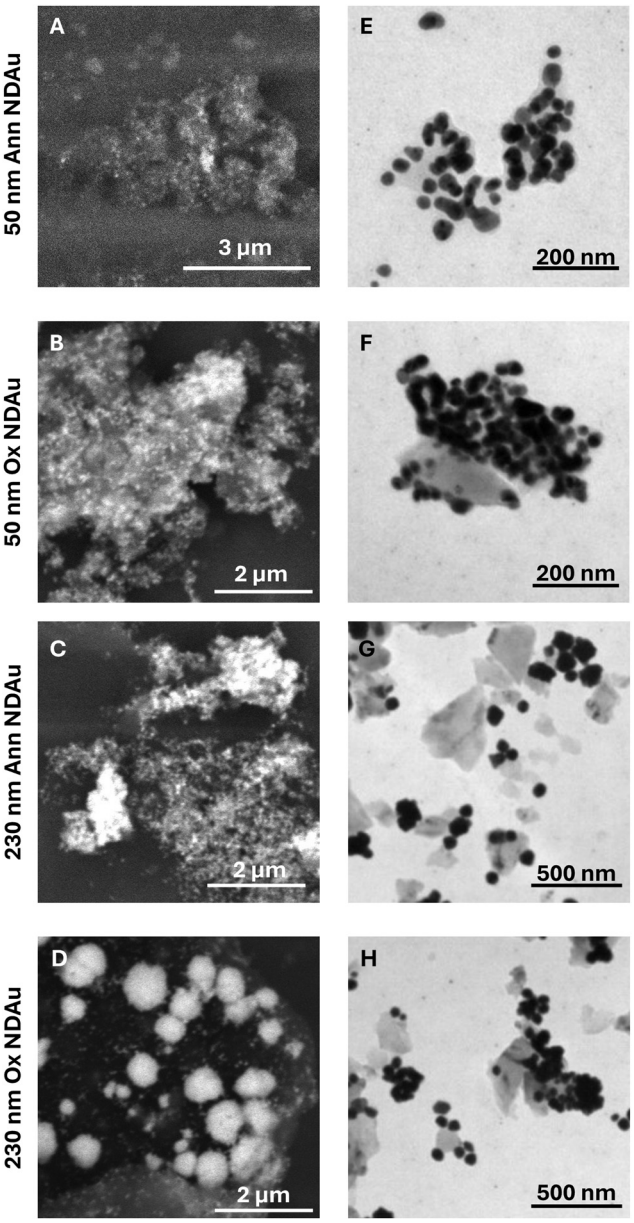

Fig. 5 SEM (left) and TEM (right) images of NDAu annealed (Ann) and oxidized (Ox). 50 nm Ann NDAu (A) and (E); 50 nm Ox NDAu (B) and (F) 230 nm Ann NDAu (C) and (G); 230 nm Ox NDAu (D) and (H).

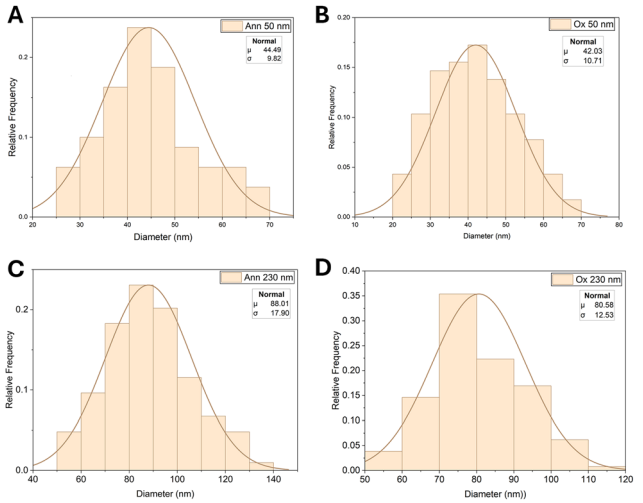

Fig. 6 Size distribution of (A) Ann 50 nm NDAu, (B) Ox 50 nm NDAu, (C) Ann 230 nm NDAu and (D) 230 nm NDAu. μ and σ represent the mean and standard deviation, respectively, of the fitted normal distribution of particle diameters.

nanoparticles are distributed across the ND surfaces. However, the extent of AuNPs coverage varied, and not all diamond surfaces were fully coated. The gold nanoparticles exhibited a broad size distribution, suggesting uncontrolled growth after nucleation on the ND surface. This lack of size regulation can be attributed to the absence of capping agents and the intrinsic non-uniformity of the ND surface, which likely influenced nucleation and growth dynamics.[67] In future studies, it would be beneficial to explore variations in both the concentration and type of plant extracts used in the synthesis of AuNPs. Adjusting these parameters can significantly influence the size, shape, and functional properties of the resulting nanoparticles.

For instance, a study by Teimuri-Mofrad *et al.* (2017) discusses the impact of different plant extracts on the green synthesis of AuNPs, highlighting how variations in extract composition can affect nanoparticle characteristics.[68] By systematically varying the extract type and concentration, we can optimize the synthesis process to tailor AuNPs for specific applications, such as drug delivery, catalysis, therapy or imaging.[44,46,68–70]

Energy dispersive X-ray spectroscopy (EDX) analysis confirmed that the NDAu were composed solely of carbon and gold, with no detectable impurities or artifacts. Red crosses in the Fig. S4–S7 indicate the locations where EDS spectra were acquired (see Fig. S4–S7 and Table S5). The ζ-potential of nanoparticles reflects the electric potential at the interface between the particle surface and the surrounding liquid medium. This potential arises from the distribution of ions around the nanoparticle, particularly within the electric double layer, and serves as a key indicator of colloidal stability. As shown in Table 5, gold coating resulted in a significant decrease in the ζ-potential of all annealed NDAu samples, shifting toward more negative values. The ζ-potential distribution of the nanodiamonds is presented in the (Table S6), providing a visualization of these variations. This trend was particularly evident for Ann NDAu 230, where the ζ-potential decreased by almost 35 mV (from −3.84 mV to −39.3 mV), compared to a decrease of around 30 mV for Ann NDAu 50 (from −26.1 mV to −56.9 mV). This change correlated with better dispersibility in suspension, suggesting that surface modification enhanced the stability of NDAu. Indeed, it is well-known that nanoparticles with high absolute ζ-potential values tend to repel each other more strongly, reducing aggregation and improving stability, while values close to 0 mV ($\pm$5 mV) indicate weaker repulsion and potential instability.[71] In contrast, the ζ-potential of Ox NDAu 50 remained relatively constant but increased for the Ox NDAu 230 batch. These variations suggest that while surface modification influences ζ-potential, factors such as particle size and surface-to-volume ratio also play a role, with smaller NDAu samples consistently exhibiting more negative ζ-potential values. The observed changes in the ζ-potential of NDAu samples can be significantly influenced by the presence of polyphenolic compounds and carboxyl groups introduced during the synthesis process. These functional groups, commonly found in plant extracts used for nanoparticle synthesis, play a crucial role in determining the surface charge and stability of nanoparticles. Polyphenols, abundant in many plant extracts, contain phenolic hydroxyl (–OH) and carboxyl (–COOH) groups. At physiological pH, these groups can deprotonate, imparting a negative charge on the nanoparticle surface. This increase in negative surface charge enhances the electrostatic repulsion between particles, thereby improving colloidal stability. For instance, a study on chitosan-functionalized hydroxyapatite nanoparticles demonstrated that polyphenols provide a negative ζ-potential due to the deprotonation of phenolic and carboxylic groups at pH 7.4, leading to increased stability of the colloidal system.[72,73] The surface charge of nanoparticles, as indicated by ζ-potential, is a critical factor in their interaction with cellular membranes. Cell membranes typically possess a net negative charge due to the presence of phospholipid bilayers. Nanoparticles with highly negative ζ-potentials may experience electrostatic repulsion, potentially reducing cellular uptake. Conversely, nanoparticles with positive ζ-potentials can interact more readily with cell membranes, facilitating uptake but also posing a risk of cytotoxicity due to membrane disruption. A study investigating polymeric nanoparticles found that those with positive surface charges exhibited stronger interactions with cells and higher cytotoxicity compared to negatively charged nanoparticles.[74–76]

Different extracts contain varying amounts and types of polyphenols and other functional groups, which can modulate

Table 5 ζ-potential of all NDs and NDAus suspended in Milli-Q (>18 MΩ) water

Sample	Zeta potential, ζ (mV)
Ann ND 50	−26.1 ± 0.6
Ox ND 50	−54.8 ± 1.8
Ann ND 230	−3.8 ± 0.2
Ox ND 230	−67.7 ± 1.1
Ann NDAu 50	−56.9 ± 1.0
Ox NDAu 50	−54.9 ± 0.2
Ann NDAu 230	−39.3 ± 0.6
Ox NDAu 230	−40.8 ± 0.8

the surface chemistry and charge of the nanoparticles, thereby impacting key aspects of NDAu stability and its interactions with cells. Given the influence of size, ζ-potential, and other physicochemical characteristics of nanoparticles on their stability and cellular interactions, understanding these surface properties is essential for evaluating NDAu's performance in biomedical applications. The colloidal stability of the NDAu samples was assessed by UV-Vis spectroscopy 0, 3, 6 and 24 hours after suspension in cell culture medium (Fig. S8). The most notable result is the red-shift of the of the characteristic gold plasmon peak, indicative of an increase in the apparent particle size.[77] This shift is attributed to the formation of a protein corona, resulting from the adsorption of biomolecules from the medium onto the NDAu surface. Notably, the red-shift is already observable at 0 h, underscoring the rapid onset of protein adsorption. Despite these changes, the gold plasmon peak remains detectable at all time points, suggesting that the particles maintain their overall integrity over 24 h. Accordingly, we investigate the biological evaluation of NDAu, focusing on cell viability by cytotoxicity assays, cell survival, clonogenic assay, and NDAu cellular uptake. These experiments offer valuable insights into the biological behavior of NDAu and their potential applications in radiosensitization and drug delivery.

Cell studies

The ATP luminescence assay was used to evaluate the cytotoxicity, in A549 cells, of the Ox NDAu 50 (1–50 μg mL^{-1}) (Fig. 7), revealing no statistically significant reduction in viability at concentrations below 20 μg mL^{-1}. This outcome is not unexpected as the biocompatibility of gold and diamond is well-established. Based on this, the survival fraction (SF) was quantified in A549 cells incubated with 10 or 20 μg mL^{-1} Ox 50 nm NDAu (Fig. 8).

The cytotoxicity of the synthesized NDAus was, also, evaluated in A549 cells incubated with oxidized and annealed NDAu 50 and NDAu 230 at concentrations ranging from 1 to 100 μg mL^{-1} MTT assays (Fig. S9 and S10). The results obtained using both the MTT and ATP luminescence assays were similar. After 24 hours of incubation, both Ox NDAu 50 and Ox NDAu 230 showed low toxicity, with cell viability relative to the controls remaining above 80% even at a concentration of 100 μg mL^{-1} (Fig. S9 and S10). Comparable results were obtained for the annealed NDAu samples (Fig. S9). However, after 48 hours of incubation, the viability of cells treated with Ann NDAu 230 had decreased significantly from 90% to below 70% (Fig. S10). This decrease in cellular viability may be attributed to the larger particle size, increased tendency to aggregate and lower dispersibility, which could lead to NDAu 230 deposition and accumulation on the surface of cells and subsequent interference with cell function.

The results of the clonogenic assay performed on A549 cells are presented in Fig. 8. The cells were incubated with Ox NDAu 50 for 24 hours, in the absence of irradiation, and following proton irradiation. The data indicate that incubation with 10 and 20 μg mL^{-1} of NDAus significantly reduced the survival fraction (SF). However, control samples incubated with NDAus maintained SF values above 60%, corresponding to a modifying factor ratio (SF without NDAus/SF with NDAus) below 1.6. Upon proton beam irradiation, the SF decreased markedly in both the control group and the NDAu-treated cells ($p < 0.001$, relative to non-irradiated counterparts). Despite the relatively high radiation dose (17 Gy), which would be expected to attenuate the radiosensitizing effect, a significant difference persisted between the SF of irradiated controls and that of cells treated

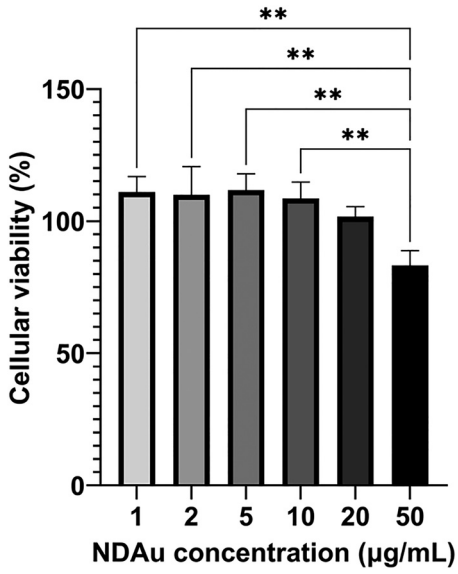

Fig. 7 Cellular viability of the A549 cell line exposed to various concentrations Ox 50 nm NDAu nanoparticles incubated for 24 hours, as measured by the ATP luminescence assay assay. Viability values are normalized to the control, and error bars represent the standard error of the mean (SE). ** corresponds to a $p < 0.005$.

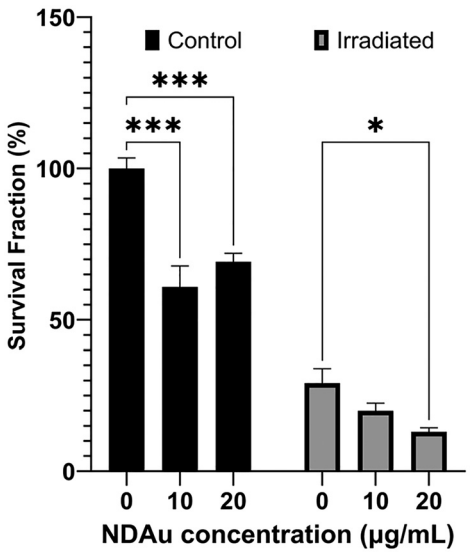

Fig. 8 Survival fraction of A549 cells incubated with 10 or 20 μg mL^{-1} Ox 50 nm NDAu prior and after proton irradiation. Results are normalized to the control, and error bars represent the standard error of the mean (SEM). *** $p < 0.001$; *$p < 0.05$.

with 20 μg mL^{-1} of Ox 50 nm NDAus, with a modifying factor ratio of 2.2. Future studies will investigate lower radiation doses to better evaluate the radiosensitizing potential of these nanoplatforms.

Cellular uptake of NDAu was evaluated using gold (Au) as a marker to localize the nanoplatform. Due to their superior biological activity, only the Ann NDAu 50 and Ox NDAu 50 samples were included in the uptake analysis. A549 cells were incubated with 20 μg mL^{-1} of Ann and Ox NDAu 50 and the results are presented in Fig. 9. Notably, Ox NDAu exhibited a more uniform Au distribution across the cell and a smoother content gradient compared to the Ann NDAu. This observation is consistent with the superior dispersibility of Ox NDAu 50 in aqueous environments. In contrast, scattered deposits of Au were observed throughout the cells treated with Ann NDAu.

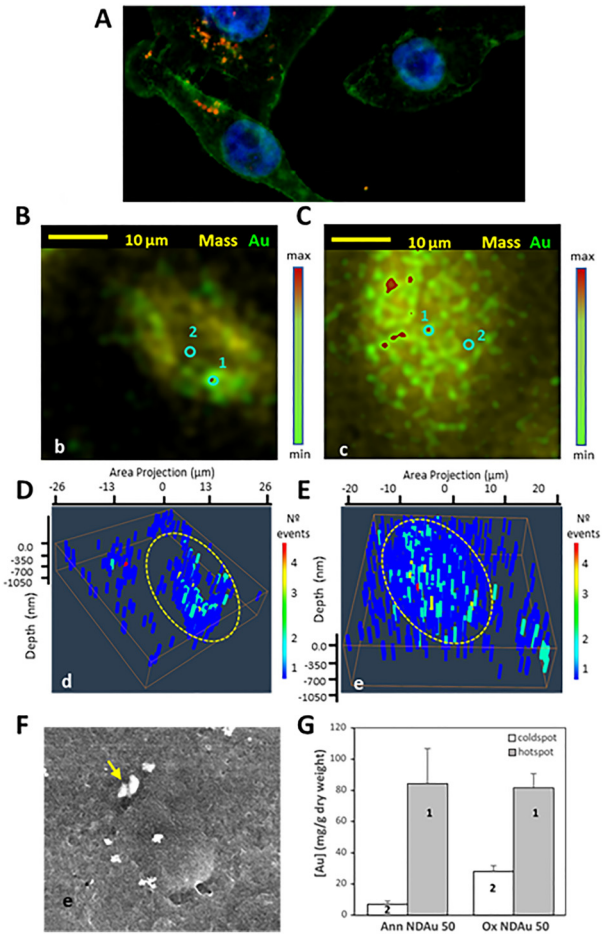

Fig. 9 (A) Fluorescence microscopy image of A549 cells incubated with 20 μg mL^{-1} Ox NDAu 50 where the NDAu particles can be visualized by their red emission (nuclei in blue and actin in green). (B) and (C) Nuclear microscopy superimposed images of mass density (STIM) and Au distribution (PIXE) in a A549 cell incubated with 20 μg mL^{-1} (B) Ann and (C) Ox NDAu 50. The gradient amount of Au is represented by a colour scale, low-green to high-red and mass distribution by a yellow gradient. (D) and (E) 3D representation of Au distribution through the depth of the cells represented in (B) and (C), given by a three-layer model of approximately 340 nm depth resolution. The zero depth is the cell surface. The amount of Au is expressed as the number of events corrected for beam energy loss at different depths (colour scale, left). (F) SEM image of A549 cells incubated with 20 μg mL^{-1} Ox NDAu 50 for 24 hours. NDAu particles with a diffuse contour (arrow) are likely internalized. (G) Au concentration (mg g^{-1} dry weight) of Ann and Ox NDAu in the hotspots and coldspots.

Quantitative analysis was performed using PIXE with matrix composition and thickness parameters derived from EBS. Au concentrations were measured at hotspots and coldspots, regions of high and low Au signal intensity respectively, illustrated in the distribution maps of Fig. 9B and C as points 1 and 2. The quantitative analysis (Fig. 9G) of multiple points across six individual cells per condition revealed distinct and significant differences in Au distribution. Cells treated with Ann NDAu 50 showed a difference in Au concentration of approximately thirteen-fold between hot and cold spots, whereas cells treated with Ox NDAu 50 showed only a three-fold difference. Specifically, in Ann NDAu 50 treated cells, the Au concentration (on a dry weight basis) was 7.0 ± 1.8 mg g^{-1} in coldspots and 84 ± 22 mg g^{-1} in hotspots ($p < 0.001$). For Ox NDAu 50, the corresponding values were 28 ± 4 mg g^{-1} and 81 ± 9 mg g^{-1} ($p < 0.001$). The Au levels in the hotspots did not differ significantly between the Ann and Ox NDAu 50 samples, indicating that these regions likely correspond to agglomerates of NDAu particles. These agglomerates appear larger in cells treated with Ann NDAu 50. However, a significantly higher Au content was found in coldspots of Ox NDAu 50 treated cells than in Ann NDAu 50 ($p < 0.01$). Three-dimensional (3D) Au distribution maps, corrected for beam energy loss at different depths obtained from EBS spectral analysis[78] (Fig. 9D and E), shows a high number of events extending across the full cellular thickness (approximately 900–1000 nm, a typical thickness for freeze-dried cells as measurements were performed in vacuum). This confirms the internalization of Au in Ox NDAu 50 treated A549 cells, and therefore more efficient nanoparticle uptake. In the Ann NDAu 50 treated cells the Au deposits mostly remain in the upper surface layers of the cell.

SEM images of A549 cells also incubated with 20 μg mL^{-1} Ox NDAu 50 (Fig. 9F), further support NDAu internalization showing distinct features of internalized aggregates compared to those on the cell surface. Taken together, the Au distribution profiles suggest enhanced dispersion of Ox NDAu, likely due to differences in surface modifications that improve dispersion and may facilitate cellular uptake, as evidenced by the more homogeneous Au distribution throughout the cellular volume compared to Ann NDAu 50.

Conclusions

In this study, we successfully synthesised a diamond-gold hybrid nanostructure (NDAu) using green chemistry. Root extracts from *Nymphaea alba* were employed as reducing agents for ionic gold. The presence of gold in the modified NDAu was corroborated using different techniques. These techniques included UV-vis, which showed the LSPR absorption band characteristic of gold nanoparticle formation; PXRD, which revealed the five gold diffraction peaks; PIXE, which determined the gold content to be near 40%; and Raman spectroscopy, which showed that the

diamond peak signal was significantly reduced due to the gold coating of the nanodiamonds. Additionally, the surface treatments performed on the pristine NDs were evident in their corresponding NDAus, with oxidised NDAus generally exhibiting greater stability and dispersibility than annealed NDAus. FTIR analysis confirmed the influence of the plant extracts, revealing absorption bands attributed to functional groups. TEM analysis showed that the average size of NDAu 50 was in the range of 40 nm, whereas that of NDAu 230 was twice as high.

Biological assays performed on A549 lung carcinoma cell line indicated that the NDAus, especially those based on oxidized NDs, were biocompatible at therapeutic concentrations and were taken up efficiently by cells. Higher cellular uptake of Ox NDAu indicates a more biologically active surface modification that can be useful for targeted therapeutic delivery or ND based radiosensitizers. Furthermore, the differences seen in the gold distribution patterns in Ann and Ox samples highlight the significant role that surface chemistry plays in dictating biological interactions. Furthermore, the efficient uptake of Ox NDAu by A549 cells resulted in enhanced proton-induced cell killing, highlighting the importance of further elucidating the mechanisms of radiosensitisation.

In summary, our findings suggest that the green-synthesized NDAu are nanoplatforms for various biomedical uses, such as bioimaging, targeted drug delivery, and radiosensitization. Their prospective application as radiosensitizers in proton therapy provides intriguing prospects for improving outcomes in cancer therapy by augmenting tumor-specific radiation damage while reducing detrimental effects on proximal healthy tissue. Future research efforts will be geared towards assessing the radiosensitizing potential of these NDAu platforms under a proton beam as well as further exploring surface modifications that could be performed on these platforms.

Author contributions

Edgar Mendes (EM): formal analysis, investigation, validation, writing the original draft, writing – review & editing; Pietro Aprà (PA): formal analysis, investigation, validation, writing – review & editing; Ana Belchior (AB): conceptualization, funding acquisition, methodology, supervision, paper administration, formal analysis, investigation, validation, resources, visualization, writing the original draft and writing – review & editing; Federico Picollo (FP): conceptualization, funding acquisition, methodology, supervision, paper administration, formal analysis, investigation, validation, resources, writing the original draft and writing – review & editing; Marta M. Alves (MMA): formal analysis, investigation, validation, resources, visualization, writing – review & editing; Rodica Mihaela Dinica (RMD): formal analysis, investigation, validation, resources, writing – review & editing; Maria João Moura (MJM): formal analysis, investigation, validation, resources, writing – review & editing; Sofia Sturari (SS): formal analysis, investigation, validation, visualization, writing – review & editing; Teresa Pinheiro (TP): conceptualization, funding acquisition, methodology, supervision, paper administration, formal analysis, investigation, validation, resources, visualization, writing the original draft and writing – review & editing; Maria Paula Cabral Campello (MPCC): conceptualization, funding acquisition, methodology, supervision, paper administration, formal analysis, investigation, validation, resources, visualization, writing the original draft and writing – review & editing. All authors have read and agreed to the published version of the manuscript.

Conflicts of interest

There are no conflicts to declare.

Data availability

The data supporting this article have been included as part of the supplementary information (SI). The supplementary information contains supplementary figures and tables related to the characterization of nanoparticles (Table S1: synthesis of NDAu Nanoplatforms; Fig. S1: UV-Vis spectrophotometry; Fig. S2: ATR-FTIR spectroscopy; Fig. S3 and Tables S2–S3: PXRD spectra and calculations; Table S4: PIXE results; Fig. S4–S7 and Table S5: SEM images and EDS results; Table S6: Zeta potential; Fig. S8: colloidal stability in cell medium) and cell viability studies (Fig. S9–S10). See DOI: https://doi.org/10.1039/d5nh00424a.

Acknowledgements

Funded by Fundação para a Ciência e Tecnologia (FCT/MEC) for projects UID/MULTI/04349/2025, PTDC/BTM-TEC/29256/2017, UIDB/04565/2020, UIDP/04565/2025 (iBB/IST), UIDP/50007/2020 (LIP), and LA/P/0140/2020 (i4HB), project UIDB/00100/2020 (https://doi.org/10.54499/UIDP/00100/2020) https://doi.org/10.54499/UIDB/00100/2020 (CQE/IST), and LA/P/0056/2020 (https://doi.org/10.54499/LA/P/0056/2020) (IMS), and by AURORA INFN projects funded by National Institute for Nuclear Physics (INFN) and the project 23NRM04 NoQTeS has received funding from the European Partnership on Metrology, cofinanced from the European Union's Horizon Europe Research and Innovation Programme and by the Participating Statesupported by the coordinated research project "Sub-cellular imaging and irradiation using accelerator-based techniques" of the International Atomic Energy Agency (IAEA, CRP F11024). The authors gratefull acknowledges DR. António P. Matos from Centro de Investigação Interdisciplinar Egas Moniz (Caparica, Portugal) for fruitful discussion on TEM studies.

Notes and references

1 B. Liu, H. Zhou, L. Tan, K. T. H. Siu and X.-Y. Guan, Exploring treatment options in cancer: tumor treatment strategies, *Signal Transduction Targeted Ther.*, 2024, **9**, 1–44.
2 R. Naser, H. Dilabazian, H. Bahr, A. Barakat and M. El-Sibai, A guide through conventional and modern cancer treatment modalities: A specific focus on glioblastoma cancer therapy (Review), *Oncol. Rep.*, 2022, **48**, 1–17.

3 C. Forenzo and J. Larsen, Bridging clinical radiotherapy and space radiation therapeutics through reactive oxygen species (ROS)-triggered delivery, *Free Radicals Biol. Med.*, 2024, **219**, 88–103.
4 R. Mohan, A review of proton therapy – Current status and future directions, *Precis. Radiat. Oncol.*, 2022, **6**, 164–176.
5 S. Yan, T. A. Ngoma, W. Ngwa and T. R. Bortfeld, Global democratisation of proton radiotherapy, *Lancet Oncol.*, 2023, **24**, e245–e254.
6 N. Priyadarshni, R. Singh and M. K. Mishra, Nanodiamonds: Next generation nano-theranostics for cancer therapy, *Cancer Lett.*, 2024, **587**, 216710.
7 V. N. Mochalin, O. Shenderova, D. Ho and Y. Gogotsi, The properties and applications of nanodiamonds, *Nat. Nanotechnol.*, 2012, **7**, 11–23.
8 J. Xu and E. K.-H. Chow, Biomedical applications of nanodiamonds: From drug-delivery to diagnostics, *SLAS Technol.*, 2023, **28**, 214–222.
9 A. Mzyk, A. Sigaeva and R. Schirhagl, Relaxometry with Nitrogen Vacancy (NV) Centers in Diamond, *Acc. Chem. Res.*, 2022, **55**, 3572–3580.
10 V. Y. Osipov, F. M. Shakhov, K. V. Bogdanov, K. Takai, T. Hayashi, F. Treussart, A. Baldycheva, B. T. Hogan and C. Jentgens, High-Quality Green-Emitting Nanodiamonds Fabricated by HPHT Sintering of Polycrystalline Shockwave Diamonds, *Nanoscale Res. Lett.*, 2020, **15**, 209.
11 J. L. Sánchez Toural, V. Marzoa, R. Bernardo-Gavito, J. L. Pau and D. Granados, Hands-On Quantum Sensing with NV− Centers in Diamonds, *C*, 2023, **9**, 16.
12 V. Benson and A. Amini, Why nanodiamond carriers manage to overcome drug resistance in cancer, *Cancer Drug Resist.*, 2020, **3**, 854–866.
13 J. Lazovic, E. Goering, A.-M. Wild, P. Schützendübe, A. Shiva, J. Löffler, G. Winter and M. Sitti, Nanodiamond-Enhanced Magnetic Resonance Imaging, *Adv. Mater.*, 2024, **36**, 2310109.
14 D. E. J. Waddington, M. Sarracanie, H. Zhang, N. Salameh, D. R. Glenn, E. Rej, T. Gaebel, T. Boele, R. L. Walsworth, D. J. Reilly and M. S. Rosen, Nanodiamond-enhanced MRI via in situ hyperpolarization, *Nat. Commun.*, 2017, **8**, 15118.
15 Z. Hou, Z. Wang, P. Wang, F. Chen and X. Luo, Near-infrared light-triggered mild-temperature photothermal effect of nanodiamond with functional groups, *Diamond Relat. Mater.*, 2022, **123**, 108831.
16 C. Angelou, I. S. Patallo, D. Doherty, F. Romano and G. Schettino, A review of diamond dosimeters in advanced radiotherapy techniques, *Med. Phys.*, 2024, **51**, 9230–9249.
17 P. Aprà, N. H. Amine, A. Britel, S. Sturari, V. Varzi, M. Ziino, L. Mino, P. Olivero and F. Picollo, Creation, Control, and Modeling of NV Centers in Nanodiamonds, *Adv. Funct. Mater.*, 2024, **34**, 2404831.
18 P. Aprà, G. Zanelli, E. Losero, N.-H. Amine, G. Andrini, M. Barozzi, E. Bernardi, A. Britel, R. Canteri, I. P. Degiovanni, L. Mino, E. Moreva, P. Olivero, E. Redolfi, C. Stella, S. Sturari, P. Traina, V. Varzi, M. Genovese and F. Picollo, Effects of Thermal Oxidation and Proton Irradiation on Optically Detected Magnetic Resonance Sensitivity in Sub-100 nm Nanodiamonds, *ACS Appl. Mater. Interfaces*, 2025, **17**, 21589–21600.
19 Z. Mi, C.-B. Chen, H. Q. Tan, Y. Dou, C. Yang, S. P. Turaga, M. Ren, S. K. Vajandar, G. H. Yuen, T. Osipowicz, F. Watt and A. A. Bettiol, Quantifying nanodiamonds biodistribution in whole cells with correlative iono-nanoscopy, *Nat. Commun.*, 2021, **12**, 4657.
20 V. Varzi, E. Fratini, M. Falconieri, D. Giovannini, A. Cemmi, J. Scifo, I. Di Sarcina, P. Aprà, S. Sturari, L. Mino, G. Tomagra, E. Infusino, V. Landoni, C. Marino, M. Mancuso, F. Picollo and S. Pazzaglia, Nanodiamond Effects on Cancer Cell Radiosensitivity: The Interplay between Their Chemical/Physical Characteristics and the Irradiation Energy, *Int. J. Mol. Sci.*, 2023, **24**, 16622.
21 X. Chen, H. Wang, H. Wang, Y. Fu, J. Liu and R. Liu, The Radiosensitizing Effect of Nanodiamonds (NDs) on HeLa Cells Under X-Ray Irradiation, *Phys. Status Solidi A*, 2018, **215**, 1700715.
22 T. Wanek, S. Mairinger, M. Raabe, M. N. A. Alam, T. Filip, J. Stanek, G. Winter, L. Xu, C. Laube, T. Weil, V. Rasche and C. Kuntner, Synthesis, radiolabeling, and preclinical *in vivo* evaluation of 68Ga-radiolabelled nanodiamonds, *Nucl. Med. Biol.*, 2023, **116–117**, 108310.
23 D. Wang, Y. Tong, Y. Li, Z. Tian, R. Cao and B. Yang, PEGylated nanodiamond for chemotherapeutic drug delivery, *Diamond Relat. Mater.*, 2013, **36**, 26–34.
24 L. Lai and A. S. Barnard, Functionalized Nanodiamonds for Biological and Medical Applications, *J. Nanosci. Nanotechnol.*, 2015, **15**, 989–999.
25 E. Alexander and K. W. Leong, Nanodiamonds in biomedical research: Therapeutic applications and beyond, *PNAS Nexus*, 2024, **3**, pgae198.
26 K. J. van der Laan, M. Hasani, T. Zheng and R. Schirhagl, Nanodiamonds for In Vivo Applications, *Small*, 2018, **14**, 1703838.
27 S. Sturari, I. Andreana, P. Aprà, V. Bincoletto, J. Kopecka, L. Mino, B. Zurletti, B. Stella, C. Riganti, S. Arpicco and F. Picollo, Designing functionalized nanodiamonds with hyaluronic acid–phospholipid conjugates for enhanced cancer cell targeting and fluorescence imaging capabilities, *Nanoscale*, 2024, **16**, 11610–11622.
28 W. Liu, B. Naydenov, S. Chakrabortty, B. Wuensch, K. Hübner, S. Ritz, H. Cölfen, H. Barth, K. Koynov, H. Qi, R. Leiter, R. Reuter, J. Wrachtrup, F. Boldt, J. Scheuer, U. Kaiser, M. Sison, T. Lasser, P. Tinnefeld, F. Jelezko, P. Walther, Y. Wu and T. Weil, Fluorescent Nanodiamond–Gold Hybrid Particles for Multimodal Optical and Electron Microscopy Cellular Imaging, *Nano Lett.*, 2016, **16**, 6236–6244.
29 S. Orlanducci, Gold-Decorated Nanodiamonds: Powerful Multifunctional Materials for Sensing, Imaging, Diagnostics, and Therapy, *Eur. J. Inorg. Chem.*, 2018, 5138–5145.
30 F. O. G. Olorundare, S. Makaluza, N. Midzi, O. A. Arotiba and D. Nkosi, A nanoDiamond/gold nanoparticle-based electrochemical immunosensor for the detection of HER 2 cancer biomarker, *Biosens. Bioelectron.: X*, 2024, **18**, 100483.
31 I. Rehor, K. L. Lee, K. Chen, M. Hajek, J. Havlik, J. Lokajova, M. Masat, J. Slegerova, S. Shukla, H. Heidari, S. Bals,

N. F. Steinmetz and P. Cigler, Plasmonic Nanodiamonds: Targeted Core–Shell Type Nanoparticles for Cancer Cell Thermoablation, *Adv. Healthcare Mater.*, 2015, **4**, 460–468.

32 F. O. G. Olorundare, S. Makaluza, N. Midzi, O. A. Arotiba and D. Nkosi, A nanoDiamond/gold nanoparticle-based electrochemical immunosensor for the detection of HER 2 cancer biomarker, *Biosens. Bioelectron.: X*, 2024, **18**, 100483.

33 I. Rehor, K. L. Lee, K. Chen, M. Hajek, J. Havlik, J. Lokajova, M. Masat, J. Slegerova, S. Shukla, H. Heidari, S. Bals, N. F. Steinmetz and P. Cigler, Plasmonic Nanodiamonds: Targeted Core–Shell Type Nanoparticles for Cancer Cell Thermoablation, *Adv. Healthcare Mater.*, 2015, **4**, 460–468.

34 L. Schmidheini, R. F. Tiefenauer, V. Gatterdam, A. Frutiger, T. Sannomiya and M. Aramesh, Self-Assembly of Nanodiamonds and Plasmonic Nanoparticles for Nanoscopy, *Biosensors*, 2022, **12**, 148.

35 F. Silva, A. Paulo, A. Pallier, S. Même, É. Tóth, L. Gano, F. Marques, C. F. G. C. Geraldes, M. M. C. A. Castro, A. M. Cardoso, A. S. Jurado, P. López-Larrubia, S. Lacerda and M. P. Cabral Campello, Dual Imaging Gold Nanoplatforms for Targeted Radiotheranostics, *Materials*, 2020, **13**, 513.

36 A. S. Schwartz-Duval, Y. Mackeyev, I. Mahmud, P. L. Lorenzi, M. Gagea, S. Krishnan and K. V. Sokolov, Intratumoral Biosynthesis of Gold Nanoclusters by Pancreatic Cancer to Overcome Delivery Barriers to Radiosensitization, *ACS Nano*, 2024, **18**, 1865–1881.

37 S. B. Shelar, K. C. Barick, B. Dutta, M. Basu and P. A. Hassan, Selective targeting of gold nanoparticles for radiosensitization of somatostatin 2 receptor-expressing cancer cells, *J. Drug Delivery Sci. Technol.*, 2023, **82**, 104381.

38 R. A. Rashid, N. N. T. Sisin, K. A. Razak, M. Geso, H. Akasaka, R. Sasaki, T. Tominaga, H. Miura, M. Nishi, A. A. Almutery and W. N. Rahman, Cell survival analysis of radiosensitization effects by gold nanoparticles for proton beam therapy, *J. Radiat. Res. Appl. Sci.*, 2025, **18**, 101203.

39 Y.-C. Lin, E. Perevedentseva, Z.-R. Lin, C.-C. Chang, H.-H. Chen, S.-M. Yang, M.-D. Lin, A. Karmenyan, G. Speranza, L. Minati, C. Nebel and C.-L. Cheng, Multimodal bioimaging using nanodiamond and gold hybrid nanoparticles, *Sci. Rep.*, 2022, **12**, 5331.

40 C. Cunningham, M. de Kock, M. Engelbrecht, X. Miles, J. Slabbert and C. Vandevoorde, Radiosensitization Effect of Gold Nanoparticles in Proton Therapy, *Front. Public Health*, 2021, **9**, 699822.

41 S.-J. Seo, J. Jae-Kun, H. Sung-Mi and J.-K. Kim, Reactive oxygen species-based measurement of the dependence of the Coulomb nanoradiator effect on proton energy and atomic Z value, *Int. J. Radiat. Biol.*, 2017, **93**, 1239–1247.

42 C.-Y. Lo, S.-W. Tsai, H. Niu, F.-H. Chen, H.-C. Hwang, T.-C. Chao, I.-T. Hsiao and J.-W. Liaw, Gold-Nanoparticles-Enhanced Production of Reactive Oxygen Species in Cells at Spread-Out Bragg Peak under Proton Beam Radiation, *ACS Omega*, 2023, **8**, 17922–17931.

43 Y. Lin, H. Paganetti, S. J. McMahon and J. Schuemann, Gold nanoparticle induced vasculature damage in radiotherapy: Comparing protons, megavoltage photons, and kilovoltage photons, *Med. Phys.*, 2015, **42**, 5890–5902.

44 A. Menichetti, A. Mavridi-Printezi, D. Mordini and M. Montalti, Effect of Size, Shape and Surface Functionalization on the Antibacterial Activity of Silver Nanoparticles, *J. Funct. Biomater.*, 2023, **14**, 244.

45 M. Cudalbeanu, I. O. Ghinea, B. Furdui, D. Dah-Nouvlessounon, R. Raclea, T. Costache, I. E. Cucolea, F. Urlan and R. M. Dinica, Exploring New Antioxidant and Mineral Compounds from Nymphaea alba Wild-Grown in Danube Delta Biosphere, *Molecules*, 2018, **23**, 1247.

46 M. Cudalbeanu, D. Peitinho, F. Silva, R. Marques, T. Pinheiro, A. C. Ferreira, F. Marques, A. Paulo, C. F. Soeiro, S. A. Sousa, J. H. Leitão, A. Tăbăcaru, S. M. Avramescu, R. M. Dinica and M. P. C. Campello, Sono-Biosynthesis and Characterization of AuNPs from Danube Delta Nymphaea alba Root Extracts and Their Biological Properties, *Nanomaterials*, 2021, **11**, 1562.

47 R. N. Morgan and K. M. Aboshanab, Green biologically synthesized metal nanoparticles: biological applications, optimizations and future prospects, *Future Sci. OA*, 2024, **10**, FSO935.

48 M. Cudalbeanu, B. Furdui, G. Cârâc, V. Barbu, A. V. Iancu, F. Marques, J. H. Leitão, S. A. Sousa and R. M. Dinica, Antifungal, Antitumoral and Antioxidant Potential of the Danube Delta Nymphaea alba Extracts, *Antibiotics*, 2019, **9**, 7.

49 H. M. Abuzeid, C. M. Julien, L. Zhu and A. M. Hashem, Green Synthesis of Nanoparticles and Their Energy Storage, Environmental, and Biomedical Applications, *Crystals*, 2023, **13**, 1576.

50 Z. Wang, Y. Huang, D. Lv, G. Jiang, F. Zhang and A. Song, Tea polyphenol-assisted green synthesis of Ag-nanodiamond hybrid and its catalytic activity towards 4-nitrophenol reduction, *Green Chem. Lett. Rev.*, 2019, **12**, 197–207.

51 M.-L. Meyer, S. Peters, T. S. Mok, S. Lam, P.-C. Yang, C. Aggarwal, J. Brahmer, R. Dziadziuszko, E. Felip, A. Ferris, P. M. Forde, J. Gray, L. Gros, B. Halmos, R. Herbst, P. A. Jänne, B. E. Johnson, K. Kelly, N. B. Leighl, S. Liu, I. Lowy, T. U. Marron, L. Paz-Ares, N. Rizvi, C. M. Rudin, E. Shum, R. Stahel, N. Trunova, P. A. Bunn and F. R. Hirsch, Lung cancer research and treatment: global perspectives and strategic calls to action, *Ann. Oncol.*, 2024, **35**, 1088–1104.

52 A. B. Buades, L. C. J. Pereira, B. J. C. Vieira, A. C. Cerdeira, J. C. Waerenborgh, T. Pinheiro, A. P. A. Matos, C. G. Pinto, J. F. Guerreiro, F. Mendes, S. Valic, F. Teixidor, C. Viñas and F. Marques, The Mössbauer effect using 57Fe-ferrabisdicarbollide ([o-57FESAN]−): a glance into the potential of a low-dose approach for glioblastoma radiotherapy, *Inorg. Chem. Front.*, 2022, **9**, 1490–1503.

53 A. V. Tyurnina, I. A. Apolonskaya, I. I. Kulakova, P. G. Kopylov and A. N. Obraztsov, Thermal Purification of Detonation Diamond.

54 P. Aprà, L. Mino, A. Battiato, P. Olivero, S. Sturari, M. C. Valsania, V. Varzi and F. Picollo, Interaction of Nanodiamonds with Water: Impact of Surface Chemistry on Hydrophilicity, Aggregation and Electrical Properties, *Nanomaterials*, 2021, **11**, 2740.

55 D. S. Volkov, P. I. Semenyuk, M. V. Korobov and M. A. Proskurnin, Quantification of nanodiamonds in aqueous solutions by spectrophotometry and thermal lens spectrometry, *J. Anal. Chem.*, 2012, **67**, 842–850.

56 A. Belchior, B. C. Alves, E. Mendes, F. Megre, L. C. Alves, P. Santos, K. Nishimura, H. Nakamura, F. Teixidor, C. Viñas, J. M. Sampaio, F. Marques and T. Pinheiro, Unravelling physical and radiobiological effects of proton boron fusion reaction with anionic metallacarboranes ([o-COSAN]-) in breast cancer cells, *EJNMMI Res.*, 2025, **15**, 13.

57 T. Pinheiro, L. C. Alves, A. P. Matos, I. Correia, J. Costa Pessoa and F. Marques, Cellular targets of cytotoxic copper phenanthroline complexes: a multimodal imaging quantitative approach in single PC3 cells, *Metallomics*, 2024, **16**, mfae051.

58 D. S. Volkov, P. I. Semenyuk, M. V. Korobov and M. A. Proskurnin, Quantification of nanodiamonds in aqueous solutions by spectrophotometry and thermal lens spectrometry, *J. Anal. Chem.*, 2012, **67**, 842–850.

59 S. A. Khan, S. B. Khan, L. U. Khan, A. Farooq, K. Akhtar and A. M. Asiri, in *Handbook of Materials Characterization*, ed. S. K. Sharma, Springer International Publishing, Cham, 2018, pp. 317–344.

60 T. Petit and L. Puskar, FTIR spectroscopy of nanodiamonds: Methods and interpretation, *Diamond Relat. Mater.*, 2018, **89**, 52–66.

61 R. Kurrey, M. K. Deb, K. Shrivas, B. R. Khalkho, J. Nirmalkar, D. Sinha and S. Jha, Citrate-capped gold nanoparticles as a sensing probe for determination of cetyltrimethylammonium surfactant using FTIR spectroscopy and colorimetry, *Anal. Bioanal. Chem.*, 2019, **411**, 6943–6957.

62 J. Robertson, Mechanical properties and structure of diamond-like carbon, *Diamond Relat. Mater.*, 1992, **1**, 397–406.

63 J. Cebik, J. K. McDonough, F. Peerally, R. Medrano, I. Neitzel, Y. Gogotsi and S. Osswald, Raman spectroscopy study of the nanodiamond-to-carbon onion transformation*, *Nanotechnology*, 2013, **24**, 205703.

64 S. Osswald, G. Yushin, V. Mochalin, S. O. Kucheyev and Y. Gogotsi, Control of sp^2/sp^3 Carbon Ratio and Surface Chemistry of Nanodiamond Powders by Selective Oxidation in Air, *J. Am. Chem. Soc.*, 2006, **128**, 11635–11642.

65 H. Pang, X. Wang, G. Zhang, H. Chen, G. Lv and S. Yang, Characterization of diamond-like carbon films by SEM, XRD and Raman spectroscopy, *Appl. Surf. Sci.*, 2010, **256**, 6403–6407.

66 D. Zhang, B. Shen and F. Sun, Study on tribological behavior and cutting performance of CVD diamond and DLC films on Co-cemented tungsten carbide substrates, *Appl. Surf. Sci.*, 2010, **256**, 2479–2489.

67 M.-C. Kim, D. Lee, S. H. Jeong, S.-Y. Lee and E. Kang, Nanodiamond–Gold Nanocomposites with the Peroxidase-Like Oxidative Catalytic Activity, *ACS Appl. Mater. Interfaces*, 2016, **8**, 34317–34326.

68 R. Teimuri-mofrad, R. Hadi, B. Tahmasebi, S. Farhoudian, M. Mehravar and R. Nasiri, Green synthesis of gold nanoparticles using plant extract: Mini-review, *Nanochem. Res.*, 2017, **2**, 8–19.

69 S. Ahmad, S. Ahmad, Q. Xu, I. Khan, X. Cao, R. Yang and H. Yan, Green synthesis of gold and silver nanoparticles using crude extract of Aconitum violaceum and evaluation of their antibacterial, antioxidant and photocatalytic activities, *Front. Bioeng. Biotechnol.*, 2024, **11**, 1320739.

70 A. Fouda, A. M. Eid, E. Guibal, M. F. Hamza, S. E.-D. Hassan, D. H. M. Alkhalifah and D. El-Hossary, Green Synthesis of Gold Nanoparticles by Aqueous Extract of Zingiber officinale: Characterization and Insight into Antimicrobial, Antioxidant, and In Vitro Cytotoxic Activities, *Appl. Sci.*, 2022, **12**, 12879.

71 S. A. Akintelu, S. C. Olugbeko and A. S. Folorunso, A review on synthesis, optimization, characterization and antibacterial application of gold nanoparticles synthesized from plants, *Int. Nano Lett.*, 2020, **10**, 237–248.

72 Polyphenols from Grape Pomace: Functionalization of Chitosan-Coated Hydroxyapatite for Modulated Swelling and Release of Polyphenols | Langmuir, https://pubs.acs.org/doi/10.1021/acs.langmuir.1c01930, (accessed 24 April 2025).

73 A. Martínez-Cuazitl, M. D. C. Gómez-García, S. Pérez-Mora, M. Rojas-López, R. J. Delgado-Macuil, J. Ocampo-López, G. J. Vázquez-Zapién, M. M. Mata-Miranda and D. G. Pérez-Ishiwara, Polyphenolic Compounds Nanostructurated with Gold Nanoparticles Enhance Wound Repair, *Int. J. Mol. Sci.*, 2023, **24**, 17138.

74 C. Liu, S. Dong, X. Wang, H. Xu, C. Liu, X. Yang, S. Wu, X. Jiang, M. Kan and C. Xu, Research progress of polyphenols in nanoformulations for antibacterial application, *Mater. Today Bio*, 2023, **21**, 100729.

75 X.-R. Shao, X.-Q. Wei, X. Song, L.-Y. Hao, X.-X. Cai, Z.-R. Zhang, Q. Peng and Y.-F. Lin, Independent effect of polymeric nanoparticle zeta potential/surface charge, on their cytotoxicity and affinity to cells, *Cell Proliferation*, 2015, **48**, 465–474.

76 A. M. Ross, R. M. Cahalane, D. R. Walsh, A. M. Grabrucker, L. Marcar and J. J. E. Mulvihill, Identification of Nanoparticle Properties for Optimal Drug Delivery across a Physiological Cell Barrier, *Pharmaceutics*, 2023, **15**, 200.

77 M. P. Monopoli, C. Åberg, A. Salvati and K. A. Dawson, Biomolecular coronas provide the biological identity of nanosized materials, *Nat. Nanotechnol.*, 2012, **7**, 779–786.

78 M. s Vasco, L. c Alves, V. Corregidor, D. Correia, C. P. Godinho, I. Sá-Correia, A. Bettiol, F. Watt and T. Pinheiro, 3D map distribution of metallic nanoparticles in whole cells using MeV ion microscopy, *J. Microsc.*, 2017, **267**, 227–236.

